Tropospheric Rossby Wave Breaking and the NAO/NAM

COURTENAY STRONG AND GUDRUN MAGNUSDOTTIR

Department of Earth System Science, University of California, Irvine, Irvine, California

(Manuscript received 30 September 2007, in final form 7 February 2008)

ABSTRACT

Objective analysis of several hundred thousand anticyclonic and cyclonic breaking Rossby waves is performed for the Northern Hemisphere (NH) winters of 1958–2006. A winter climatology of both anticyclonic and cyclonic Rossby wave breaking (RWB) frequency and size (zonal extent) is presented for the 350-K isentropic surface over the NH, and the spatial distribution of RWB is shown to agree with theoretical ideas of RWB in shear flow.

Composites of the two types of RWB reveal their characteristic sea level pressure anomalies, upper- and lower-tropospheric velocity fields, and forcing of the upper-tropospheric zonal flow. It is shown how these signatures project onto the centers of action and force the velocity patterns associated with the North Atlantic Oscillation (NAO) and Northern Hemisphere annular mode (NAM). Previous studies have presented evidence that anticyclonic (cyclonic) breaking leads to the positive (negative) polarity of the NAO, and this relationship is confirmed for RWB over the midlatitudes centered near 50°N. However, an opposite and statistically significant relationship, in which cyclonic RWB forces the positive NAO and anticyclonic RWB forces the negative NAO, is shown over regions 20° to the north and south, centered at 70° and 30°N, respectively.

On a winter mean basis, the frequency of RWB over objectively defined regions covering 12% of the area of the NH accounts for 95% of the NAO index and 92% of the NAM index. A 6-hourly analysis of all the winters indicates that RWB over the objectively defined regions affects the NAO/NAM without a time lag. Details of the objective wave-breaking analysis method are provided in the appendix.

1. Introduction

Rossby waves depend upon a nonzero background potential vorticity (PV) gradient for their restoring mechanism. When the background latitudinal PV gradient is small, large-amplitude Rossby waves may break, resulting in the mixing of PV over a longitudinally confined region, the wave-breaking region. Rossby wave breaking (RWB) is manifested by the large-scale and rapid irreversible overturning of PV contours on isentropic surfaces (McIntyre and Palmer 1985). We are interested in the effects of these events on the general circulation. For tropospheric flows, we have closely examined large-scale events that break anticyclonically in a hierarchy of model simulations (Walker and Magnusdottir 2002; Walker and Magnusdottir 2003, and references therein) and in reanalysis data (Abatzoglou and Magnusdottir 2006a). Examples of both anticyclonic and cyclonic RWB are shown in Figs. 1a and 1b, respectively. The primary motivation for the above-cited studies was the possibility of nonlinear reflection out of the wave-breaking region and back into the midlatitudes, thus affecting the extratropical wave field directly. We detected nonlinear reflection following breaking in approximately a third of all events (Abatzoglou and Magnusdottir 2006a), and we found that winter breaking over the North Atlantic has an opposite effect on the North Atlantic Oscillation (NAO) depending on whether or not the RWB results in reflection (Abatzoglou and Magnusdottir 2006b). In all cases, we only considered anticyclonic events because we were studying the direct effects of RWB (i.e., wave–mean flow interaction with the existence of a reflected wave train), and anticyclonic RWB is more likely to result in reflection.

Here we extend this line of work in two ways to include the indirect effects of breaking on the atmospheric general circulation (i.e., wave–mean flow interaction with or without the existence of a reflected wave

Corresponding author address: Dr. Courtenay Strong, Department of Earth System Science, University of California, Irvine, Irvine, CA 92697-3100.
E-mail: cstrong@uci.edu

DOI: 10.1175/2008JAS2632.1

© 2008 American Meteorological Society

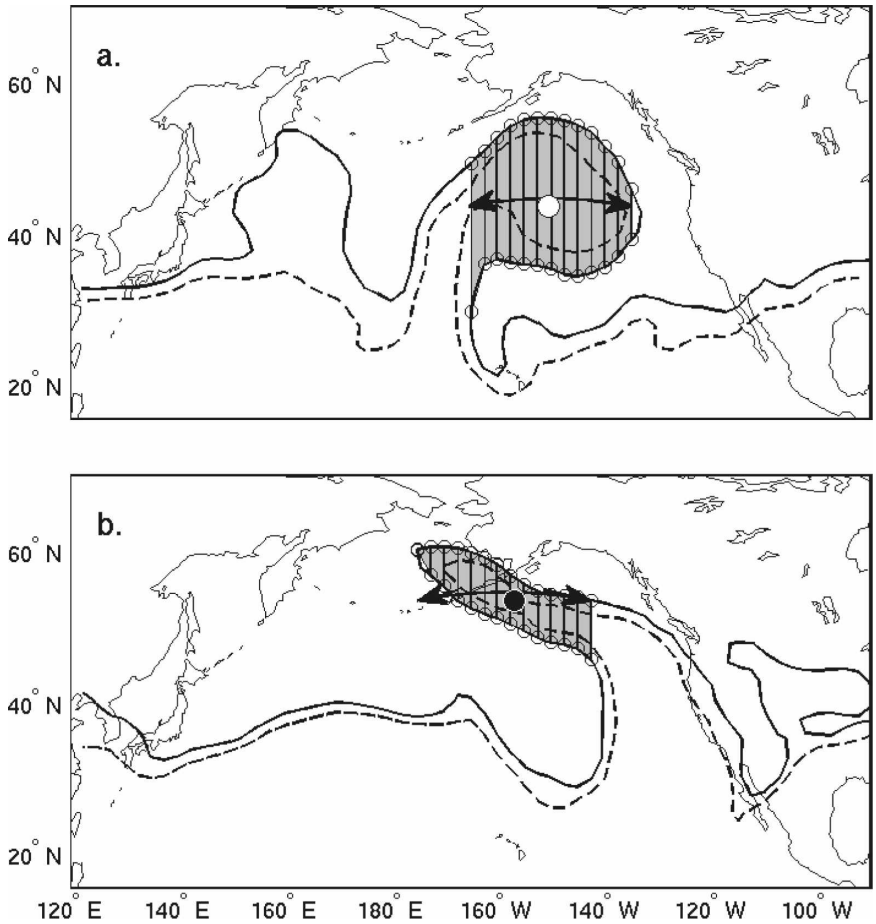

FIG. 1. The shading indicates the area and the curves with double arrows indicate the zonal extent of the break. (a) The 3- (dashed) and 5-pvu (solid) contours at 350 K at 1200 UTC 22 Jan 2002. The large filled circle marks the centroid of the anticyclonic break's poleward-advected tongue. (b) Same as (a) but for 4.5- (dashed) and 6-pvu (solid) contours at 1800 UTC 21 Jan 2001, and the large open circle marks the centroid of the cyclonic break's poleward advected tongue.

train). First, we consider the entire Northern Hemisphere (NH) troposphere rather than the midlatitude to subtropical tropopause region. Second, we consider cyclonic and anticyclonic breaking. To accomplish these goals, we develop a novel algorithm that allows us to detect and distinguish cyclonic and anticyclonic breaking on any isentropic surface throughout the NH. Details of the method are described in the appendix.

The difference between the two types of RWB, anticyclonic and cyclonic, becomes particularly clear in baroclinic life cycle simulations (e.g., Thorncroft et al. 1993; Magnusdottir and Haynes 1996). These studies found that anticyclonically breaking life cycle (LC1) is associated with an equatorward-directed pseudomomentum flux, whereas cyclonically breaking life cycle (LC2) is associated with a poleward-directed pseudomomentum flux. Eddy stirring, which occurs when RWB takes place, forces the NAO on intraseasonal time scales (e.g., Wittman et al. 2005; Vallis et al. 2004). Abatzoglou and Magnusdottir (2006a) confirmed in reanalysis data that the stirring associated with anticyclonic RWB is associated with increased pseudomomentum flux toward the latitude of breaking (equatorward), such that there is convergence of the flux into the wave-breaking region with divergence elsewhere. Anticyclonic RWB is always accompanied by increased momentum flux; however, increased momentum flux does not always signify RWB because localized linear Rossby wave propagation has the signature of increased momentum flux. Therefore, in examining the effect on the mean flow arising from RWB, it is essential to diagnose the wave breaking first and then examine the resulting signature in momentum flux.

Several recent observational studies have examined RWB (or its related signature) as it influences the NAO. Using high-frequency eddy momentum flux as a proxy for RWB, Riviere and Orlanski (2007) present evidence that anticyclonic (cyclonic) wave breaking is associated with a poleward (equatorward) shift in the jet stream over the Atlantic, leading to the positive (negative) polarity of the NAO. Previously, Benedict et al. (2004) had examined the synoptic signatures of several cases of NAO positive and negative evolution and found that they were associated with RWB. Woollings et al. (2008) studied the prolonged (i.e., five days or longer) blocking-like PV gradient reversals that sometimes follow RWB over the North Atlantic and found these reversals to be more frequent (infrequent) during the negative (positive) polarity of the NAO. Martius et al. (2007) found significant differences in the spatial distribution of PV streamers dependent on the polarity of the NAO, in which the two types of PV streamers (Wernli and Sprenger 2007) represent late stages in the two baroclinic life cycles, LC1 and LC2. Strong and Magnusdottir (2008) recently demonstrated how anticyclonic RWB over the Pacific influences the development of the NAO.

Here, we diagnose winter RWB in instantaneous 6-hourly reanalysis data, extending over 49 winters. Data and methods are presented in section 2. We distinguish between anticyclonic and cyclonic types of RWB and present an NH climatology of the geographical distribution of wave-breaking frequency of each type during the winter season in section 3. We develop composites of anticyclonic and cyclonic RWB events by shifting the analyzed fields in space and time so that they align, revealing the characteristic signatures of each of the two types of wave breaking as they force the mean flow in section 4a. Furthermore, by considering the latitude of breaking, we emphasize the effect of different latitudinal locations of RWB in terms of influencing the mean flow in section 4b. In section 5, we use correlation to objectively define the geographical regions where cyclonic and anticyclonic RWB most strongly projects onto the NAO/Northern Hemisphere annular mode (NAM). In section 6a, we use RWB frequency in the objectively defined regions to develop a multivariate linear statistical model, which accounts for more than 90% of the variance of the winter mean NAO index (NAOI) and the NAM index (NAMI; also called the Arctic Oscillation index). In section 6b, we perform a 6-hourly analysis to show that RWB over the objectively defined regions affects the NAO/NAM without a time lag. Section 7 contains a summary and brief concluding remarks.

2. Data and methods

As RWB takes place, the PV overturning may be anticyclonic (Fig. 1a) or cyclonic (Fig. 1b), depending in part on the local fields of shear and deformation (e.g., Hartmann and Zuercher 1998). We introduce a method (described in the appendix) for identifying overturning PV contours on isentropic surfaces to investigate the effect of wave breaking on the NAO. We applied the method on four upper-tropospheric and lower-stratospheric surfaces: 330, 350, 400, and 450 K. We found that the results on 350 K provide a useful representation of upper-tropospheric anticyclonic and cyclonic breaking over all latitudes because higher-latitude RWB structures are deep enough to be detected by higher PV values on this surface. Moreover, RWB frequency at the 350-K level is well correlated with variability in the NAO and NAM. Breaking on the 400- and 450-K levels was contaminated by pure stratospheric breaking, whereas considerably fewer events were captured on 330 than on 350 K for both types of breaking.

a. Data and analysis of wave breaking

We use PV and the horizontal components of the velocity field at 6-hourly temporal and 2.5° spatial resolution on the 350-K isentropic surface from National Centers for Environmental Prediction–National Center for Atmospheric Research (NCEP–NCAR) reanalysis data for winters from December 1958 to February 2006 (DJF). We use the National Oceanic and Atmospheric Admistration (NOAA) Climate Prediction Center Arctic Oscillation index as our NAMI. It is constructed by projecting daily 1000-hPa geopotential height anomalies poleward of 20°N onto the leading empirical orthogonal function (EOF) of monthly-mean 1000-hPa geopotential for the 1979–2000 period. From the NCAR Climate and Global Dynamics Division, we use a NAOI based on the leading EOF of sea level pressure anomalies over the Atlantic sector (20–80°N, 90°W–90°E).

Our wave-breaking detection method objectively identifies the poleward-advecting low-PV tongues associated with anticyclonically and cyclonically overturning PV contours as shown in Fig. 1 (the method can alternatively be used to track and measure equatorward-advecting high-PV tongues). Our method for identifying the tongues (detailed in the appendix) is based on circumpolar PV contours that signal PV overturning by crossing a particular meridian more than once (as marked by small open circles in Fig. 1). Locating where a PV contour crosses a meridian more than once (also used by Esler and Haynes 1999) is con-

ceptually similar to searching for locations where the meridional PV gradient is negative (e.g., Abatzoglou and Magnusdottir 2006a), and the use of circumpolar contours ensures that isolated pockets of low-PV air are not mistaken for PV overturning. Using the geometry of the overturning PV contour (as opposed to gridded PV values) allows us to quantify the break's spatial scale and distinguish between anticyclonic and cyclonic overturning as shown in Fig. 1.

The low-PV tongues are identified for anticyclonic and cyclonic events at each 6-hourly observation, and the following three quantities are calculated for each tongue: the area shown by shading in Fig. 1; the location of the centroid, shown by large circles in Fig. 1; and the zonal extent (L). Here, L is defined as the degrees of arc length along a great circle route beginning at the west edge of the tongue at the latitude of the tongue's centroid and extending to the east edge of the tongue (the measured routes are shown by the curves between the double arrows in Figs. 1a,b). We adopt a minimum size criterion for the PV overturning cases included in this study (see the appendix) so that cases of marginal overturning are not included. The PV intrusions into the tropics that Waugh and Polvani (2000) studied are, for example, not counted as RWB in the present study unless they result in overturning of PV contours.

b. Defined variables

The 350-K isentropic surface over the NH is divided into $N = 400$ equally sized bins of area $\sim 6.4 \times 10^5$ km^2 using a recursive zonal equal-area sphere-partitioning algorithm (Leopard 2006). For each bin centered on $(\lambda, \phi)_n$, where $n = 1, \ldots, N$, we calculate the relative frequency of breaking centroids γ, which is a dimensionless quantity given by

$$\gamma(\lambda, \phi)_n \equiv \frac{1}{T} \sum_{t=1}^{T} \beta[(\lambda, \phi)_n, t], \tag{1}$$

where λ is longitude, ϕ is latitude, T is the number of 6-hourly observations in the period for which γ is calculated, and the event parameter $\beta[(\lambda, \phi)_n, t]$ is 1 when a centroid is located in the bin at time t but zero otherwise. Subscripts a and c are used to denote results for anticyclonic (γ_a) and cyclonic (γ_c) relative frequencies, respectively, and values for γ_a and γ_c are calculated for each winter month from December 1958 to February 2006. Note that γ is the fraction of observation times for which PV overturning is observed at a location (to be distinguished from a count of wave-breaking events in which a wave-breaking event has a certain time extent).

We also calculate the mean zonal extent of the low-PV tongues observed in each bin

$$\overline{L}(\lambda, \phi)_n \equiv \frac{1}{\sum_t \beta} \sum_{t=1}^{T} L[(\lambda, \phi)_n, t], \tag{2}$$

where $L = \beta = 0$ when no break is present in the bin. Subscripts are used to denote results for anticyclonic ($\overline{L}_a$) and cyclonic ($\overline{L}_c$) mean zonal extents, and $\overline{L}$ is given in units of arc length along a great circle route.

c. Multiple linear regression

Multivariate linear regression (MLR) models of the NAMI and NAOI are presented in section 6a using a set of indices, each of which represents the count of RWB instances over an objectively defined region of the NH. In the MLR models, the NAMI (or NAOI) and wave-breaking indices each have one value for each winter. The anticyclonic and cyclonic index regions are identified based on the correlation between the NAMI and the local time series of γ_a and γ_c calculated for each winter. More specifically, we locate local maxima of $|r(\gamma, \text{NAMI})| \geq 0.3$, where r is the Pearson correlation coefficient, and then radiate outward from these maxima at 0.1 increments of $|r|$ as long as most of the incrementally aggregated area has a significant correlation with the NAMI. Once the anticyclonic and cyclonic index regions are defined, each wave-breaking index is the DJF count of RWB centroids within the region. The DJF counts are denoted $\Sigma_{\text{DJF}}\gamma_a$ for anticyclonic and $\Sigma_{\text{DJF}}\gamma_c$ for cyclonic, and the resultant indices each have one value for each winter. We select a subset of the wave-breaking indices that is statistically appropriate for the MLR model by bootstrapping a backward stepwise regression. For bootstrapping, we use the Akaike information criterion (AIC) and determine which predictors were retained in at least 60% of the trials—a method demonstrated to produce parsimonious models with excellent predictive capability (Austin and Tu 2004).

d. Within-season analysis of NAOI transitions

To analyze how wave-breaking frequency varies with the NAO on a 6-hourly basis, we identified time periods when NAOI sign reversal occurred. Adapting the method of Kidson and Watterson (1999), we apply a low-pass filter to the 6-hourly NAOI, retaining most of the energy associated with periods of 10 days or longer. We then identified two classes of transitions: 1) "P-class" transitions occur when the filtered NAOI transitioned up from a negative local minimum to a positive local maximum and 2) "N-class" transitions occur when the filtered NAOI transitioned down from a positive local maximum to a negative local minimum. Requiring the absolute value of the filtered NAOI to be greater than 0.4 at the local maxima and local minima flanking

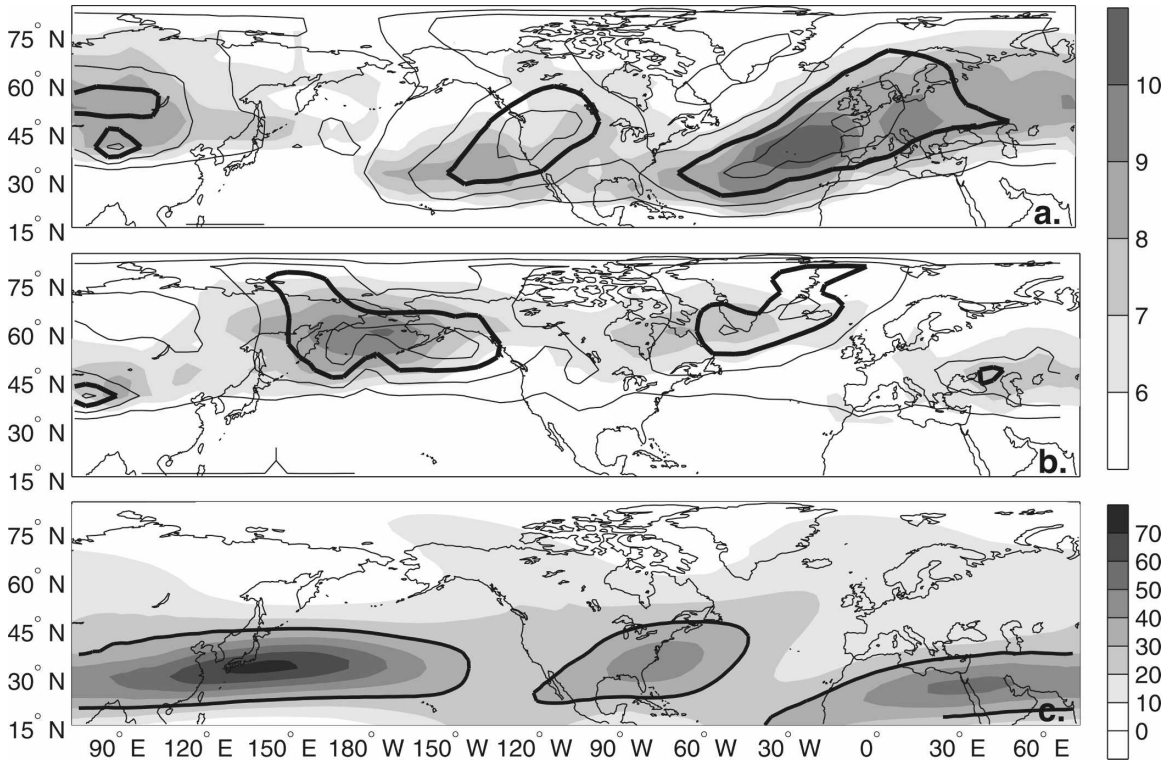

FIG. 2. (a) Anticyclonic wave-breaking for winters 1958–2006 (γ_a is contoured with interval of 0.01; the 0.03 contour is bold), and the mean zonal extent of breaks ($\overline{L}_a$ is shaded; in arc length units) along a great circle route. (b) Same as (a), except for cyclonic breaking (γ_c is contoured, $\overline{L}_c$ is shaded). (c) Mean 350-K zonal wind speed (shading intervals = 10 m s^{-1}; the 30-m s^{-1} contour is bold).

the transition yielded 52 P-class transitions and 51 N-class transitions. For each transition, the 6-hourly NAOI and centroid count in the regions objectively defined for the MLR model (section 2c) were linearly interpolated onto a time axis normalized to run from zero to one. For the N-class transitions, the local maximum was set at 0.25 and the local minimum at 0.75. For the P-class transitions, the time axis was also normalized to run from zero to one, but the local minimum was set at 0.25 and the local maximum at 0.75.

3. Climatology of anticyclonic and cyclonic RWB in winter

We show our winter RWB climatology (Figs. 2a,b) with the 350-K mean zonal wind ($\overline{u}_{350\ \mathrm{K}}$; Fig. 2c) to illustrate how the climatology follows logically from theoretical ideas of RWB in shear flow. The relative frequency of anticyclonic and cyclonic RWB is contoured (γ_a in Fig. 2a and γ_c in Fig. 2b), and the mean zonal extent of anticyclonic and cyclonic RWB ($\overline{L}_a$ in Fig. 2a and $\overline{L}_c$ in Fig. 2b) is shaded. For both anticyclonic and cyclonic RWB, there is a significant positive correlation between γ and $\overline{L}$, meaning that breaks occurring in regions of high breaking frequency (wave-breaking regions, also called surf zones) tend to have larger-than-average zonal extents.

Beginning with results for anticyclonic breaking, regions of relatively high γ_a and $\overline{L}_a$ (anticyclonic surf zones) are centered near the west coasts of North America and Europe (Fig. 2a), downstream of the jet maxima (Fig. 2c). The Atlantic anticylonic surf zone extends eastward across Asia near 60°N within the anticyclonic shear on the equatorward flank of the eddy-driven jet (this jet is shown in Fig. 1a of Strong and Davis 2007). Anticyclonic breaking in winter is more frequent over the Atlantic and involves larger-scale events than anticyclonic breaking over the Pacific (also noted by Abatzoglou and Magnusdottir 2006a).

The three primary cyclonic surf zones indicated by high γ_c and $\overline{L}_c$ in Fig. 2b are situated within the cyclonic shear poleward and downstream of the three $\overline{u}_{350\mathrm{K}}$ maxima in Fig. 2c. Areas of high γ_c are especially prevalent over the two ocean basins where the storm tracks are located and, relative to the Atlantic, the Pacific cyclonic surf zone is more expansive and contains larger-scale breaks. The longitudinal offset between the γ_a and γ_c maxima over each basin indicates that, as waves propagate eastward from the continents to the

oceans, cyclonic RWB tends to take place upstream from the location of anticyclonic RWB in faster background flow. The cyclonically breaking Rossby waves tend to have smaller spatial scales and faster phase speeds than the anticyclonic waves. The longitudinal offset between the γ_c and γ_a maxima is therefore consistent with nonlinear Rossby wave critical layer theory of small-amplitude Rossby waves on a basic-state shear flow where breaking occurs at the critical line, which is where the phase speed of the waves matches the background flow speed (Killworth and McIntyre 1985; Haynes 1989). Furthermore, Randel and Held (1991) found in atmospheric observations that upper-tropospheric eddies break and force the zonal flow approximately 10°–20° latitude before reaching their critical lines. Regions of frequent breaking tend to be collocated with regions of weak PV gradients (not shown) because breaking generally leads to PV mixing, and the low background flow speeds associated with weak PV gradients are conducive to wave breaking.

The picture of the anticyclonic breaking climatology shown in Fig. 2a is generally consistent with Abatzoglou and Magnusdottir (2006a, their Fig. 5b), even though they use a different algorithm for detecting RWB, which results in fewer RWB counts. In particular, the interesting longitudinal asymmetry in DJF anticyclonic breaking frequency between the Pacific and Atlantic was noted in their study. Note that anticyclonic RWB is almost absent from the west Pacific in winter. Abatzoglou and Magnusdottir (2006a) discussed the seasonal evolution of anticyclonic RWB frequency, and they connected the lack of west Pacific breaking in winter to the strong jet and the associated strong latitudinal PV gradient on the anticyclonic flank of the east Pacific jet stream (not shown but the jet structure is shown in Fig. 2c). All anticyclonic events north of 45°N were neglected in Abatzoglou and Magnusdottir (2006a). This means that the downstream and poleward-tilted regions of anticyclonic RWB at the end of the storm tracks were not counted, nor was the region of anticyclonic breaking over central Asia near 90°E. Additionally, Abatzoglou and Magnusdottir (2006a) used daily averaged data (as opposed to the 6-hourly observations in the present study), and they counted RWB events, which persisted in time, so that they neglected overturned PV contours that were found close in time to a previously diagnosed occurrence.

The results in Fig. 2 also have features in common with other wave-breaking climatologies that used yet other analysis methods. The regions of high γ_a in Fig. 2a, for example, overlap with regions where Martius et al. (2007) show a high frequency of anticyclonic PV streamers (LC1 events in their Fig. 5). The RWB climatology in Fig. 3c of Hitchman and Huesmann (2007) identifies regions of frequent and strong PV overturning at 350 K during DJF that overlap with our high γ_a and γ_c regions.

4. General RWB effects on the NAO/NAM

We developed anticyclonic and cyclonic RWB composites to show their respective fields of upper- and lower-tropospheric velocity, sea level pressure, and the forcing of the upper-tropospheric zonal flow (presented in section 4a). We also separated the cyclonic and anticyclonic RWB composites by region (e.g., Asia, east Pacific, and east Atlantic), latitude, and tongue area, and we found the results to be scaled but qualitatively similar (not shown). Although the local anomalies generated by breaking are to some degree regionally invariant, the location where a break occurs critically determines how it interacts with the background flow and affects circulation patterns, including the NAO/NAM. This sensitivity to location is examined further in section 4b, where we consider schematically the effects of different latitudinal locations of RWB on the NAO/NAM, and in section 5, where we show the longitudinal locations where RWB most strongly affects the NAO/NAM.

a. Anticyclonic and cyclonic composites of RWB

For each instance of RWB during winters 1958–2006, we calculated the fields of surface and 350-K velocity anomalies $\mathbf{v}' = (u', v')$ and sea level pressure anomalies p', where the prime indicates deviation from a time mean. The time mean at each location was taken over a certain calendar day and certain time of observation for the 49-yr record. We also calculated the $\mathbf{E}$ vector (Hoskins et al. 1983) for each event, where $\mathbf{E} \equiv (v'^2 - u'^2, -u'v')$. Under quasigeostrophic scaling, the quantity $\nabla \cdot \mathbf{E}$ appears in the time mean zonal momentum equation as a useful measure of the forcing (acceleration if positive) of the zonal flow associated with transient eddies (see appendix A in Hoskins et al. 1983).

We composited values of u', v', $\nabla \cdot \mathbf{E}$, and p' for anticyclonic and cyclonic RWB, such that the fields were centered on the centroid of each poleward-advecting low-PV tongue. Breaks included in the composites (Fig. 3) were required to have similar size characteristics to ensure spatial alignment of their important features: 1) a tongue area of at least 15×10^{-4} as a fraction of earth's surface area (corresponding to approximately 765 097 km^2 or 15% of the shaded area in Fig. 1a) and 2) a tongue zonal extent of 10°–15° of arc length along a great circle route (which averages to

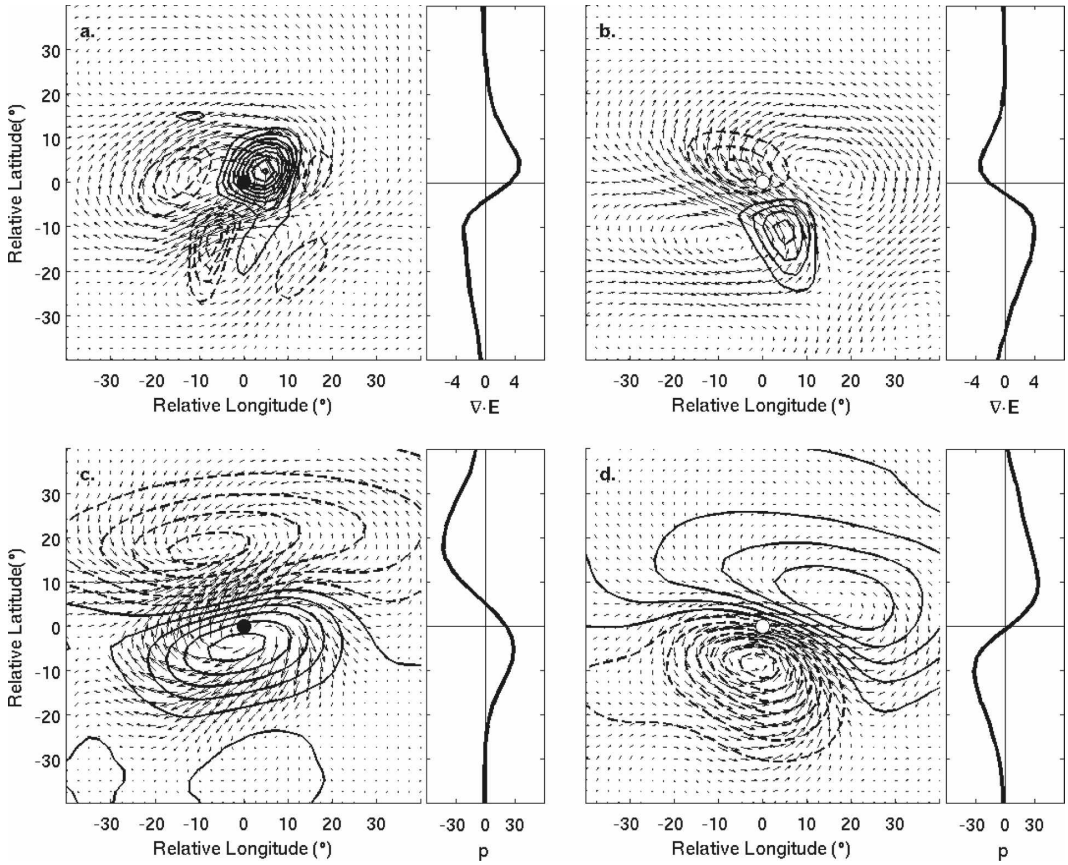

FIG. 3. Composite kinematic fields for several thousand winter wave-breaking instances in 1958–2006. (a), (c) Anticyclonic cases 30°–60°N. (b), (d) Cyclonic cases 45°–60°N. (a), (b) Composite $\nabla \cdot \mathbf{E}$ contoured at 5×10^{-5} m s^{-2} with negative values dashed and the zero contour suppressed. Composite horizontal velocity $\mathbf{V}' \equiv (u', v')$ on the 350-K isentropic surface (arrows). Fields were centered on each wave breaking centroid (depicted as the origin) prior to their inclusion in the composite. The curves to the right of (a) and (b) show the composite (limited) longitudinal average $\nabla \cdot \mathbf{E}$ (10^{-5} m s^{-2}) calculated by averaging each case from $-30°$ to 30° relative longitude and then averaging across all cases. (c), (d) Sea level pressure anomalies (contoured every 10 hPa) and horizontal velocity anomalies at lowest analysis level (σ = 0.995) and the limited longitudinal average sea level pressure (curves to right, in hPa).

approximately 1390 km or 65% of the zonal extent shown in Fig. 1a). In addition to the size restrictions, the anticyclonic composite is restricted to breaks between 30°–60°N to reflect the primary anticyclonic surf zones (Fig. 2a), and the cyclonic composite is limited to events between 45°–75°N to reflect the primary cyclonic surf zones (Fig. 2b). Following these criteria, the cyclonic composite represents approximately 12 000 cases, and the anticyclonic composite represents approximately 19 000 cases.

Each type of breaking has a 350-K anticyclonic circulation anomaly about the negative PV anomaly in its poleward tongue and a cyclonic circulation anomaly about the positive PV anomaly in its equatorward tongue (that can be inferred from the composite $\mathbf{v}'$ fields; Figs. 3a,b). The long axes of these circulation anomalies are tilted southwest to northeast for anticyclonic RWB and northwest to southeast for cyclonic RWB, contributing to the following important difference in the $\nabla \cdot \mathbf{E}$ fields: for anticyclonic RWB, the zonal flow is accelerated to the northeast and decelerated to the southwest of the centroid, whereas for cyclonic events, the flow is accelerated to the southeast and decelerated to the northwest of the centroid. The curves on the right side of the upper panels in Fig. 3 summarize the effect of RWB on the zonal flow averaged over nearby longitudes. For anticyclonic RWB, the zonal flow is accelerated north of the latitude of breaking and decelerated south of that latitude. For cyclonic RWB, the zonal flow is decelerated north of the latitude of breaking and accelerated south of that latitude. At the surface, the composite anticyclonic RWB is flanked to the south by a positive surface pressure anomaly and an anticyclonic circulation anomaly, and the RWB is

flanked to the north by a negative pressure anomaly and a cyclonic circulation anomaly (Fig. 3c). Similar features flank the composite cyclonic RWB, but they are of the opposite sense to the anticyclonic composite (i.e., lower pressure and cyclonic circulation to the south; higher pressure and anticyclonic circulation to the north; Fig. 3d). The curves on the right side of the lower panels in Fig. 3 summarize the effect of RWB on sea level pressure averaged over nearby longitudes.

b. Importance of the latitude of RWB

The composites in the preceding section indicate that RWB generates a surface pressure anomaly and, at the same time, forces the upper-tropospheric flow. The location of RWB and its sense of rotation (whether it is anticyclonic or cyclonic) determine how its pressure signature projects onto the centers of action of the NAO/NAM and how its velocity signature forces the circulation patterns associated with the positive or negative polarity of the NAO/NAM. Figure 4 illustrates the preceding ideas in a schematic by superimposing the composite anticyclonic and cyclonic RWB anomalies from Fig. 3 onto the NAO centers of action and flow pattern.

When an anticyclonic centroid occurs near 50°N (as shown in the center portion of Fig. 4a), the flanking sea level pressure anomalies project positively onto the NAO/NAM centers of action (positive on positive; negative on negative), immediately increasing the NAOI or NAMI. At the same time, the forcing of the zonal flow associated with the break (arrows in Fig. 4) is consistent with the positive polarity of the NAO/NAM (i.e., right-facing arrows occur at latitudes with solid gray lines; left-facing arrows occur at latitudes with dashed gray lines). Shifting the anticyclonic centroid 20° to the north or south [to 70° (left portion of Fig. 4a) or 30°N (right portion of Fig. 4a)] places the RWB sea level pressure signature so it projects negatively onto the NAO/NAM centers of action (negative on positive; positive on negative) and provides upper-tropospheric forcing of the zonal flow that is consistent with the negative polarity of the NAO/NAM (i.e., right-facing arrows occur at latitudes with dashed gray lines; left-facing arrows occur at latitudes with solid gray lines).

When a cyclonic centroid occurs at 50°N (as shown in the center portion of Fig. 4b), the flanking sea level pressure anomalies project negatively onto the NAO/NAM centers of action (positive on negative; negative on positive), immediately decreasing the NAOI or NAMI. At the same time, the zonal flow forcing associated with the RWB is consistent with the negative polarity of the NAO/NAM (i.e., right-facing arrows occur at latitudes with dashed gray lines; left-facing arrows occur at latitudes with solid gray lines). Shifting the cyclonic centroid 20° to the north or south [to 70° (left portion of Fig. 4b) or 30°N (right portion of Fig. 4b)] places the RWB sea level pressure anomaly fields so they project positively onto the NAO/NAM centers of action (negative on negative; positive on positive) and provides upper-tropospheric forcing of the zonal flow that is consistent with the positive polarity of the NAO/NAM (i.e., right-facing arrows occur at latitudes with solid gray lines; left-facing arrows occur at latitudes with dashed gray lines).

When the centroids are aligned along latitudes intermediate to 30°, 50°, or 70°, their sea level pressure anomalies are out of alignment with the centers of action of the NAM or NAO (their projection onto the EOF is minimal), and the forcing of the zonal flow is out of alignment with the latitude belts where the zonal wind is most strongly correlated with the NAM or NAO. The latitude where the RWB projects optimally onto the NAM or NAO is somewhat dependent on the spatial scale of the break and the longitude of occurrence but, as we show in the following sections, zonally elongated bands where RWB frequencies strongly correlate with the index are consistent with the conceptual picture that is presented schematically in this section.

5. Regions where RWB affects the NAO/NAM

We use correlation analysis to identify the regions where RWB most strongly projects onto the NAO/NAM. The correlation between the NAMI averaged over each winter (DJF) and the RWB frequency γ calculated at each point for each winter is shown in Fig. 5, where shading indicates significance at the 95% confidence level. Figure 5a shows the correlation between anticyclonic RWB frequency (γ_a) and the NAMI, and Fig. 5b shows the correlation between cyclonic RWB frequency (γ_c) and the NAMI. Correlation between anticyclonic RWB frequency and the NAMI (Fig. 5a) is strong over the Atlantic and surrounding continents. The downstream influence throughout northern Asia is especially noticeable. The weak correlation over most of the Pacific is generally collocated with low values of γ_a (Fig. 2a). The high correlation between γ_a and the NAMI over much of the Atlantic consists of a positive belt near 50°N flanked by regions of negative correlation. This $r(\gamma_a, \text{NAMI})$ tripole over the Euro-Atlantic area suggests that the latitudinal migration of the Atlantic surf zone is an important component of the relationship between the NAMI and anticyclonic wave breaking. A similar tripole appears in the leading EOF of γ_a, producing a principle component that is highly and significantly correlated with the NAM and NAO indices (not shown).

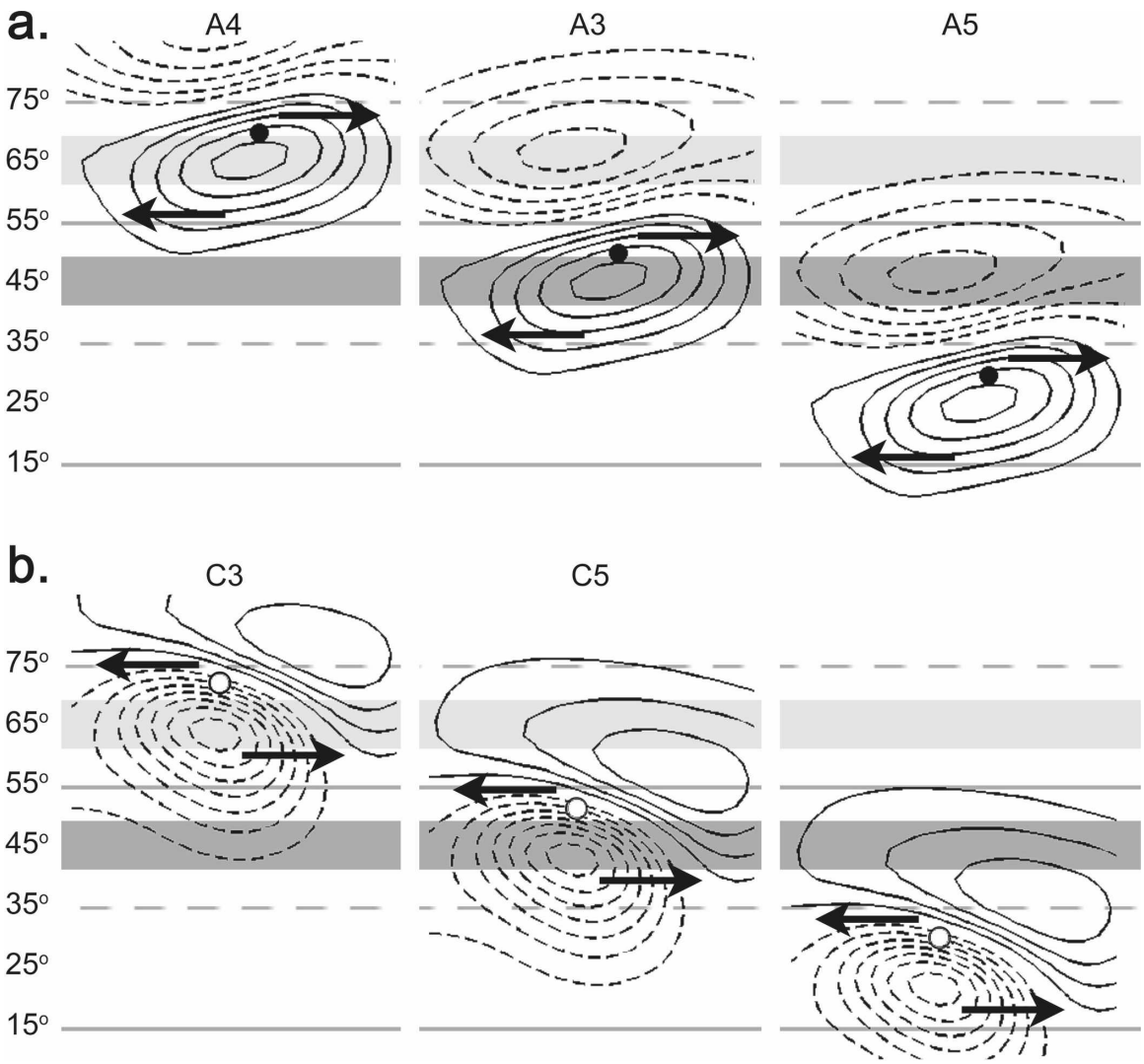

FIG. 4. Schematic (lat–lon plots) illustrating how RWB projects onto the NAO as a function of the latitude of RWB. The shaded bands at 45° and 65°N mark the centers of action of the NAO's zonally averaged EOF (dark indicates positive). Over the domain of the NAO, the zonally averaged zonal wind is most strongly negatively correlated with the NAO in bands centered at 35° and 75°N (dashed) and most strongly positively correlated with the NAO in bands centered at 15° and 55°N (solid). Labels A4, A3, A5, C3, and C5 correspond to NH regions to be identified in section 5. (a) Anticyclonic RWB centered at three different latitudes, the anticyclonic centroid (filled circle), and surrounding composite sea level pressure anomaly contours (dashed indicates negative) from Fig. 3 are displayed to scale. Right- (left) facing arrows originate at the local maximum (minimum) of the anticyclonic breaking $\nabla \cdot \mathbf{E}$ field in Fig. 3 and indicate strengthening (weakening) of the zonal flow. (b) Same as (a) but for the cyclonic composites in Fig. 3.

For cyclonic RWB (Fig. 5b), a prominent latitudinal dipole in correlation is present over the mid- to high-latitude Atlantic (or a weak tripole if the positive correlation over the Atlantic near 30°N is included), suggesting that the latitudinal migration of this cyclonic surf zone has an important connection to the NAMI. For the cyclonic RWB over the Pacific, a longitudinal dipole pattern in the correlation with the NAMI is located near 55°N, suggesting that longitudinal variations in the surf zone have a connection to the NAMI. Indeed, the leading EOF of γ_c has a similar configuration over the northern Pacific (not shown).

Following the method described in section 2c, we use the correlations in Fig. 5 to objectively define regions where RWB affects the NAO/NAM. The resulting regions are shown in Fig. 6. In addition to providing statistical evidence of the configurations presented schematically in the preceding section, these regions will yield the wave-breaking indices used in the time series analyses in section 6. Regions developed from γ_a have

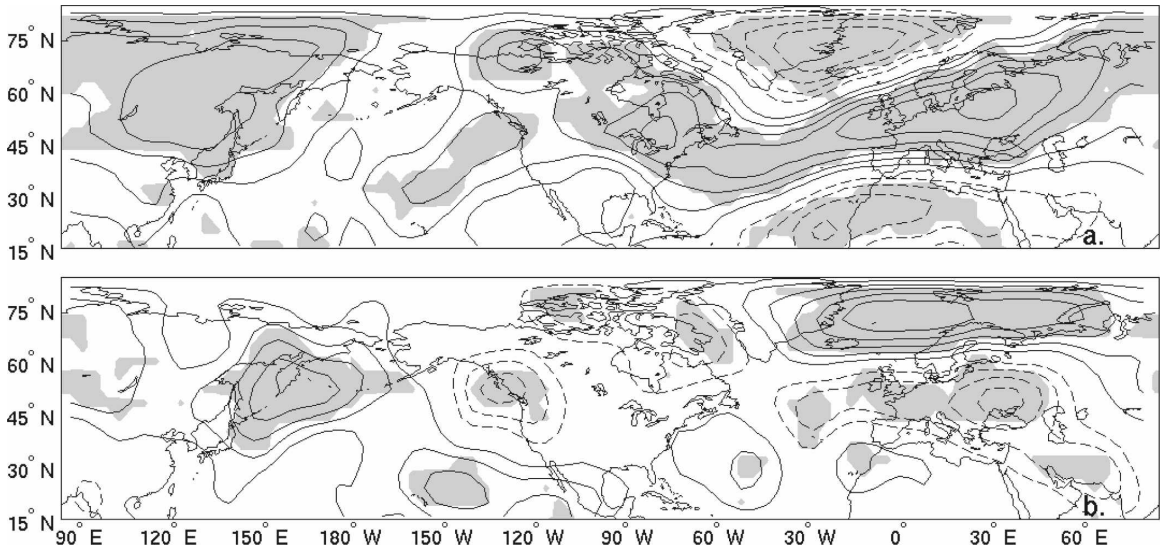

FIG. 5. (a) Pearson correlation coefficient r for regression of γ_a (frequency of anticyclonic RWB) vs NAMI, contoured at 0.1 with negative values dashed and the zero contour suppressed. Shading indicates significance at the 95% confidence level based on bootstrapping. (b) Same as (a) but for γ_c (frequency of cyclonic RWB) vs NAMI.

the prefix A, and regions developed from γ_c have the prefix C. Using region A1 as an example to establish a convention for terms, "region A1" refers to the bounded area on the map (Fig. 6a) and "A1" refers to the wave-breaking index from region A1, which is the time series of $\Sigma_{\mathrm{DJF}}\gamma_a$ from region A1 as described in section 2c. Repeating the correlation analysis using the NAOI and restricting the analysis to the Euro-Atlantic sector produces regions almost identical to regions A3, C3, A4, A5, and C5 [all located within the Euro-Atlantic sector (not shown)], which we denote by affixing a prime to each (e.g., region A3′).

Wave breaking in the regions in Fig. 6a (Fig. 6b) force the positive (negative) polarity of the NAMI in accordance with the concepts developed in section 4. For example, regions C3 and A3 correspond to the so-

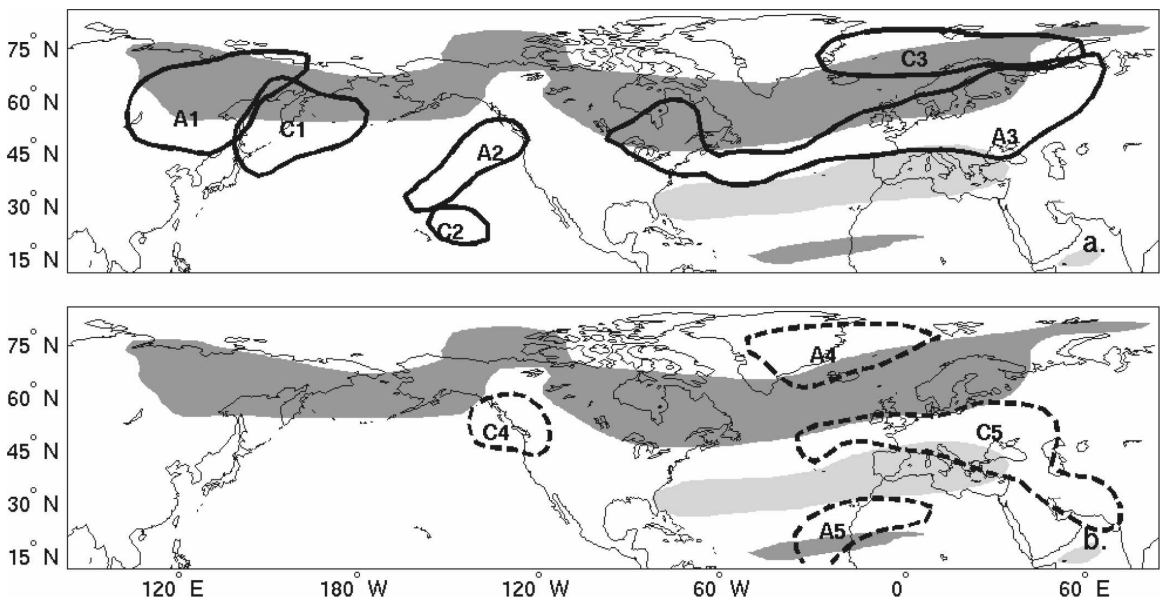

FIG. 6. Regions where RWB strongly influences NAMI (bold contours; details in text). Regions where RWB and NAMI are (a) positively or (b) negatively correlated. Dark (light) shading in each panel shows where the correlation between the zonal wind speed on the 350-K surface and NAMI is greater than 0.5 (less than −0.5).

TABLE 1. Pearson correlation coefficient r for regressions involving NAMI and time series of breaking frequency from the domains in Fig. 6. Results significant at the 95% confidence level are shown in bold.

	A1	A2	A3	A4	A5	C1	C2	C3	C4	C5
A2	0.09	—	—	—	—	—	—	—	—	—
A3	**0.59**	**0.33**	—	—	—	—	—	—	—	—
A4	−0.05	**−0.28**	**−0.49**	—	—	—	—	—	—	—
A5	**−0.34**	−0.17	**−0.64**	**0.35**	—	—	—	—	—	—
C1	**0.63**	0.10	**0.58**	−0.06	**−0.37**	—	—	—	—	—
C2	−0.05	**0.66**	**0.27**	**−0.44**	−0.22	0.10	—	—	—	—
C3	**0.56**	**0.32**	**0.75**	**−0.46**	**−0.38**	**0.62**	**0.24**	—	—	—
C4	−0.15	**−0.68**	**−0.31**	0.14	0.18	**−0.34**	**−0.57**	**−0.31**	—	—
C5	**−0.35**	**−0.36**	**−0.57**	**0.49**	0.17	**−0.37**	**−0.28**	**−0.54**	0.18	—
NAMI	**0.59**	**0.49**	**0.89**	**−0.63**	**−0.51**	**0.55**	**0.41**	**0.81**	**−0.45**	**−0.64**

labeled schematic configurations in Fig. 4 and project positively onto the NAO/NAM center of action near 65°N. This reinforces the zonal flow near 55°N but decelerates the flow near 35°N for A3 and near 75°N for C3. Regions A5 and C5 (Fig. 6b) produce an opposite effect, projecting negatively onto the NAO/NAM center of action near 45°N and accelerating (decelerating) the zonal flow near 35°N (15° and 55°N, respectively).

For the objectively identified regions, the sign of the correlation between the DJF mean NAMI and the RWB indices (Table 1) generally follows logically from the direction of the influence derived from the above analysis. For example, A3 is positively correlated with the NAMI, and anticyclonic RWB in region A3 is conducive to the positive polarity of the NAM (i.e., has a sea level pressure anomaly that projects positively onto the EOF of the NAM and a $\nabla \cdot \mathbf{E}$ anomaly pattern that forces the zonal wind anomaly pattern associated with the positive polarity of the NAM). Following the pattern of reasoning given for A3 above, corresponding observations can be made about the sign of the correlations between the NAMI and anticyclonic breaking in the other A regions and cyclonic breaking in regions C2–C5. The positive correlation between C1 and the NAMI is an interesting exception. Considering the zonal extent of the positive sea level pressure anomaly field associated with cyclonic breaking (see composite field in Fig. 3d), cyclonic breaking in C1 projects positively onto the NAM's Pacific center of action near 165°W (not shown). However, the associated $\nabla \cdot \mathbf{E}$ anomalies weaken the zonal wind in the darkly shaded region to the northwest of C1 (Fig. 6a). This deceleration is adverse to the circulation pattern associated with the positive polarity of the NAM, but it is, at least in part, offset on a seasonal mean basis by the acceleration provided by increases in A1 during winters with above-average NAMI.

Relative to the Atlantic RWB regions, the Pacific RWB regions in winter are less zonally expansive (compare basins in Figs. 6a,b); have a weaker correlation with the NAMI (Table 1); and are, in some cases, at odds in terms of their zonal wind forcing (e.g., A1 and C1 per the discussion above). The flow over the Pacific in winter is not conducive to RWB that forces the negative polarity of the NAM (compare the spatial coverage of dashed regions between the Pacific and Atlantic in Fig. 6b). These observations may provide a physical explanation for previous studies (Deser 2000; Ambaum et al. 2001), showing that the temporal coherence between Arctic and midlatitude circulation variability is stronger over the Euro-Atlantic area than over the Pacific and that the correlations between the Pacific and Atlantic midlatitudes are weak within the context of the NAM.

6. Time series analysis

This section begins with a statistical analysis to show that breaking in a subset of the regions defined above accounts for almost all of the NAOI/NAMI on an interannual basis. A within-season analysis is presented in section 6b to show that the NAO varies contemporaneously (i.e., zero time lag) with RWB frequency, which is consistent with the discussion of the composite and schematic in section 4.

a. Interannual analysis

Details of the multivariate linear models presented in this section are given in section 2c. The dependent variables of the two models are the DJF mean NAMI and NAOI. The independent variables are the wave-breaking indices A1–A5 and C1–C5 defined in section 5 as the counts of RWB in objectively defined regions. The last row of the correlation matrix in Table 1 shows that each of the regions individually provides a wave-breaking index that is a significant predictor of the NAMI. The strong correlation r(A3, NAMI) = 0.89 cannot be attributed entirely to the effect of antic-

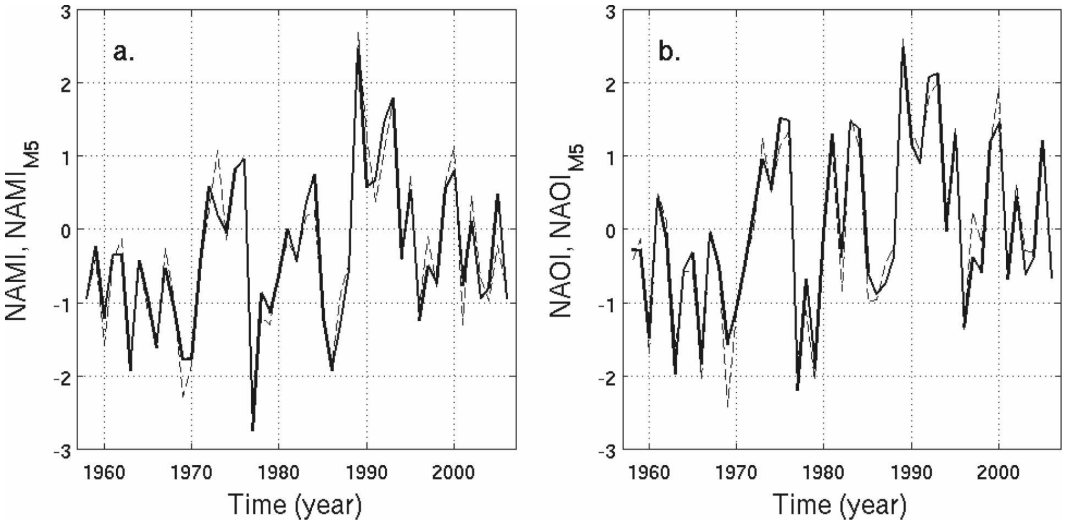

FIG. 7. (a) The $NAMI_{M5}$ statistical model (solid line) of NAMI (dashed line). (b) Same as (a) but for $NAOI_{M5}$ and NAOI.

clonic breaking in region A3. Rather, above-average γ_a in region A3 tends to occur with other conditions favorable to positive NAM polarity, that is, above-average A1, A2, and C3, and below-average A4, A5, C4, and C5 (significant correlations are bold in Table 1). Working together in the opposite direction, below-average γ_a in region A3 tends to occur with conditions adverse to the positive polarity of the NAM, that is, below-average A1, A2, and C3, and above-average A4, A5, C4, and C5. The significant correlations between breaking in the Pacific and Atlantic (e.g., A1, A2, and A3) suggest that interbasin connectivity across North America plays a role in the NAM. This connectivity is considered in more detail in Strong and Magnusdottir (2008).

For the NAMI, the bootstrap predictor selection procedure, which is described in section 2c, yields a five-predictor model denoted $NAMI_{M5}$,

$$NAMI_{M5} = 0.20(A1) + 0.49(A3) - 0.31(A4) + 0.19(C3) - 0.20(C4) - 0.36, \quad (3)$$

which accounts for 92% of the NAMI. The model fit is quite good, as shown in Fig. 7a. Even a single-predictor model using only A3 would account for nearly 80% of the NAMI. For the NAOI, the bootstrap predictor selection procedure yielded the five-predictor model $NAOI_{M5}$,

$$NAOI_{M5} = 0.74(A3') - 0.24(A4') - 0.12(A5') + 0.11(C3') - 0.17(C5') + 0.02, \quad (4)$$

which accounts for 95% of the NAOI (the fit is shown in Fig. 7b).

b. *Within-season analysis*

The interannual analysis in the preceding section illustrates the strength of the correlation between RWB and the NAO/NAM on a seasonal mean basis, but it does not consider their variation on synoptic time scales or any time lags that may be present. To supplement the interannual findings, we use 6-hourly data to consider within-season variations following the method for analyzing downward N-class and upward P-class transitions of the NAOI as described in section 2d. For the N-class and P-class transitions, we developed five composite time series as shown in Fig. 8: the NAOI, the counts of RWB within the A3′ and C3′ Euro-Atlantic regions where RWB projects positively onto the NAO, and the A5′ and C5′ Euro-Atlantic regions where RWB projects negatively onto the NAO (these regions were defined in section 5). For the N-class composite (Figs. 8a,b), the time between the local maximum and local minimum of the NAOI ranged from 3 to 20.75 days with an average of 9.2 days. The N-class local maximum of the NAOI (normalized time 0.25) is associated with maximal breaking in regions A3′ and C3′ (Fig. 8a) and minimal breaking in regions A5′ and C5′ (Fig. 8b). As the NAOI transitions from positive to negative, breaking frequency decreases in regions A3′ and C3′ while increasing in regions A5′ and C5′. Once the NAOI reaches its N-class local minimum (normalized time 0.75), breaking frequency is minimized (maximized) in regions A3′ and C3′ (A5′ and C5′). The wave-breaking indices A3′, C3′, A5′, and C5′ (Figs. 8a,b) account for the N-class NAOI in a multivariate regression with an R^2 of 0.93.

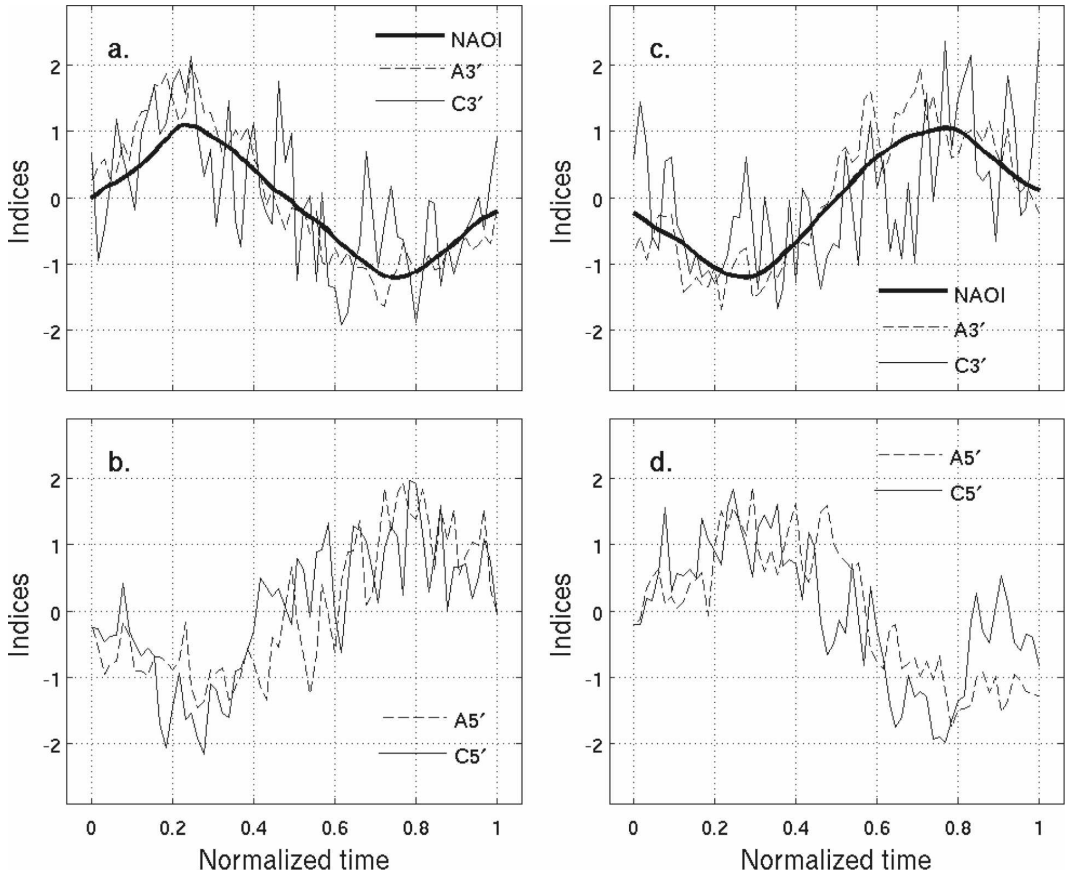

FIG. 8. Standardized composite time series of NAOI and wave-breaking indices from A3′, C3′, A5′, and C5′ regions for (a), (b) negative transitions of NAOI and (c), (d) positive transitions of NAOI.

For the P-class (Figs. 8c,d), the time between the local minimum and local maximum ranged from 4.75 to 21.5 days with an average of 8.72 days. The P-class local minimum of the NAOI resembles the N-class local minimum (i.e., maximal breaking in regions A5′ and C5′ with minimal breaking in regions A3′ and C3′). The transition to higher values of the NAOI is associated with increasing (decreasing) A3′ and C3′ (A5′ and C5′), and the local maximum P-class NAOI resembles the N-class local maximum, that is, maximal (minimal) RWB in regions A3′ and C3′ (A5′ and C5′). In Figs. 8c and 8d, the composite wave-breaking indices predict the P-class NAOI with an R^2 of 0.96.

7. Summary and concluding remarks

We introduced an objective method for detecting, measuring the size, and determining the sense of rotation of upper-tropospheric RWB, and we applied the method to 49 boreal winters of reanalysis data. The resulting RWB climatology at 350 K follows logically from theoretical ideas of RWB in shear flow, featuring frequent and large-scale anticyclonic breaking within the anticyclonic shear at the termini of the hemisphere's major jet streams. Frequent and large cyclonic RWB is situated near the storm tracks within the cyclonic shear downstream and poleward of the jet streams cores over the Pacific and Atlantic. The longitudinal offset between the γ_c and γ_a maxima was shown to be consistent with nonlinear Rossby wave critical layer theory of small-amplitude Rossby waves on a basic-state shear flow where breaking occurs at the critical line, which is where the phase speed of the waves matches the background flow speed. Results were compared to previous studies that used different methods for detecting RWB.

RWB frequencies over five objectively defined regions were used to account for more than 90% of the NAO/NAMI on an interannual basis using winter mean data and also on an intraseasonal basis using 6-hourly composites of cases in which the NAOI underwent a nontrivial sign reversal. A physical explanation for these strong statistical relationships was presented using a composite analysis of the sea level pressure

anomalies, surface- and upper-tropospheric velocity fields, and zonal wind forcing associated with thousands of instances of anticyclonic and cyclonic RWB. Superimposing the composite anomalies onto the EOF and circulation patterns associated with the NAO/NAM revealed the importance of a breaking wave's sense of rotation and latitude in determining how the break interacts with the mean flow and how it impacts NAO-like variability patterns.

Specifically, both anticyclonic and cyclonic RWB can force the positive or negative polarity of the NAM or NAO depending on their latitude. This finding is important in the context of previous observational studies (e.g., Riviere and Orlanski 2007; Benedict et al. 2004) that showed anticyclonic RWB leading to the positive NAO and cyclonic RWB leading to the negative NAO. Our analysis confirms the previously reported finding that anticyclonic RWB is associated with positive NAO when it occurs over the midlatitudes near 50°N (and the reverse for cyclonic RWB), but it shows statistically significant and opposite relationships in which cyclonic RWB forces the positive NAO, and anticyclonic RWB forces the negative NAO over regions 20° to the north and south (centered at 70° and 30°N, respectively) in latitude ranges where RWB is frequent. We thus conclude that the latitude of RWB and the sense of rotation of the breaking (anticyclonic or cyclonic) together determine its forcing of the NAM/NAO.

We found that winters with above-average NAMI tend to have above-average frequencies of anticyclonic breaking over the Pacific and Atlantic (i.e., A2 and A3 are both significantly correlated with the NAMI). Previous studies of the NAM (Deser 2000; Ambaum et al. 2001) have shown that the temporal coherence between Arctic and midlatitude variability is stronger over the Euro-Atlantic area than over the Pacific and that the correlations between the Pacific and Atlantic midlatitudes are weak. Here, we build on these previous findings by noting that the Pacific has limited RWB mechanisms available for forcing the negative polarity of the NAM and that, relative to the Atlantic RWB regions, the Pacific RWB regions are less zonally-expansive, have weaker correlation with the NAMI, and are in some cases at odds in terms of their zonal wind forcing.

Acknowledgments. We thank Ian G. Watterson for his careful review of an earlier version of the manuscript. We also thank Gwendal Riviere and Tim Woollings for their suggestions and comments on the manuscript. This work was supported by NOAA Grant NA06OAR4310149.

APPENDIX

Wave Breaking Detection

The wave-breaking detection process begins with contouring PV on the isentropic surface of interest at 0.5-PVU (1 PVU $\equiv 10^{-6}$ m^2 s^{-1} K kg^{-1}) intervals over all values of PV present on the surface. Although the full observed range of PV is contoured for completeness, most breaks at 350 K are detected over the narrower range $1.5 \leq \mathrm{PV} \leq 7$ PVU. At each PV value, constructed contours are ordered by length, and the longest circumpolar contour is retained, with the circumpolar requirement preventing an analysis of isolated pockets of high- or low-PV air not associated with wave breaking. Portions of two circumpolar contours are shown in each panel of Fig. 1, with other contours suppressed for clarity.

In regions without wave breaking, meridians intersect each PV contour only once (e.g., near Japan in Fig. 1a), reflecting a monotonic increase of PV with respect to latitude. Where wave breaking is occurring, by contrast, PV decreases locally poleward ($\partial \mathrm{PV}/\partial y < 0$) and meridians intersect circumpolar contours of PV more than once, indicating quasi-horizontal overturning of PV and, given sufficient spatial scale, wave breaking. The 160°W meridian, for example, intersects the solid circumpolar contour three times in Figs. 1a and 1b. Along meridians where more than one intersection occurs, the two intersections bounding the longest segment of relatively low PV are recorded (segments bounded by small open circles in Fig. 1).

Each set of so-identified longitudinally contiguous intersections demarcates a polygon (poleward-advecting low-PV tongue potentially associated with wave breaking) for which three quantities are calculated: the area (shading in Figs. 1a,b), the location of the centroid (large circles in Figs. 1a,b), and the zonal extent (double arrows in Figs. 1a,b). To determine if the break is cyclonic or anticyclonic, we order the points defining the contour to progress generally eastward along the contour. Referring to the examples in Fig. 1, if the latitude of the first open circle encountered running along the breaking contour is higher (lower) than the last open circle encountered, then the event is anticyclonic (cyclonic).

The specifics of the spatial-scale screening criterion are informed by the distributions of two measures of tongue geometry: 1) ℓ_c, the radius of a circle whose area matches that of the tongue, and 2) ℓ_z, half the zonal extent of the tongue ($\ell_c \rightarrow \ell_z$ as the shape of the tongue becomes more circular, and each measure is in degrees of arc length along a great circle route). The distribu-

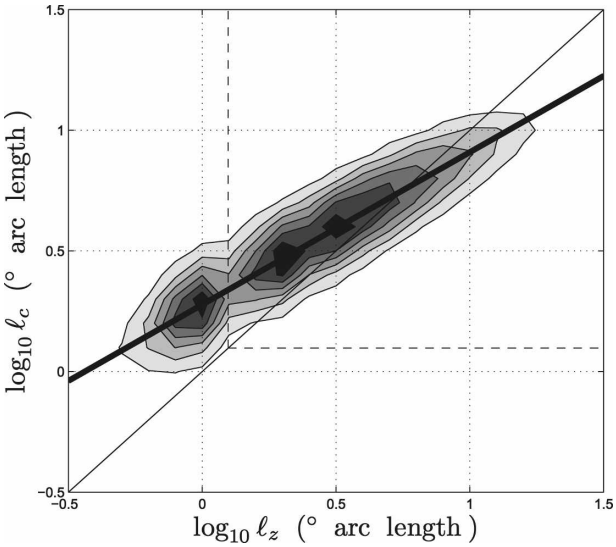

FIG. A1. Contours of binned point density in log–log space of ℓ_c vs ℓ_z , where 5% of the data reside outside the first contour. The thin sloped line indicates $\ell_c = \ell_z$, the bold sloped line is a least-squares linear regression of ℓ_c vs ℓ_z, and the dashed lines bound a box where $\log_{10}\ell \geq 0.0986$.

tion of points in the log–log space of ℓ_c versus ℓ_z (Fig. A1) indicates a class of small-scale features clustered close to $\log_{10}\ell_z = 0$. These small-scale features tend to be meridionally elongated ($\ell_c > \ell_z$) with a limited zonal extent ($2\ell_z \approx 2°$). An example of this feature is the slightly overturned contour near 40–50°N, 170°E in Fig. 1a where overturning is detected at two contiguous meridians, but the feature is not indicative of irreversible overturning and wave breaking. Noting the presence of these small-scale features in our data, and identifying $\log_{10}\ell_z \geq 0.0986$ and $\log_{10}\ell_c \geq 0.0986$ as a naturally occurring division in the ℓ_z–ℓ_c space, we retain centroids representing breaks in the upper-right box bounded by dashed lines in Fig. A1.

Concerning the redundancy criterion, the 0.5-pvu contouring interval used here may result in more than one contour tracing a single low-PV tongue, leading to at least one redundant centroid. The tongue near 150°W in Fig. 1a, for example, is traced by the 3- and 5-pvu contours. To ensure that each tongue is represented by exactly one centroid at each observation time in the dataset, we identify the centroid of the largest tongue at an observation time and eliminate any centroids within a distance equal to the lesser of ℓ_c and ℓ_z. Using the lesser of ℓ_c and ℓ_z prevents the unwarranted elimination of a centroid marking a unique tongue far to the north or south (east or west) of a longitudinally elongated (latitudinally elongated) tongue. The "ℓ-criterion" elimination is then applied sequentially to all remaining centroids ordered by decreasing tongue size.

It is the elimination of redundant centroids that enables the comprehensive analysis over the full range of PV, providing a potentially global (hemispheric in this application) view of wave breaking. The map of the mean value of PV at which wave breaking is observed on the 350-K surface for winters (DJF) 1958–2006 (not shown) resembles the PV climatology for the same period, showing zonally oriented bands increasing poleward from 1 to 7 or 8 pvu.

REFERENCES

Abatzoglou, J. T., and G. Magnusdottir, 2006a: Planetary wave breaking and nonlinear reflection: Seasonal cycle and interannual variability. *J. Climate,* **19,** 6139–6152.

——, and ——, 2006b: Opposing effects of reflective and nonreflective planetary wave breaking on the NAO. *J. Atmos. Sci.,* **63,** 3448–3457.

Ambaum, M. H. P., B. J. Hoskins, and D. B. Stephenson, 2001: Arctic Oscillation or North Atlantic Oscillation? *J. Climate,* **14,** 3495–3507.

Austin, P. C., and J. V. Tu, 2004: Bootstrap methods for developing predictive models. *Amer. Stat.,* **58,** 131–137.

Benedict, J. J., S. Lee, and S. B. Feldstein, 2004: Synoptic view of the North Atlantic Oscillation. *J. Atmos. Sci.,* **61,** 121–144.

Deser, C., 2000: On the teleconnectivity of the "Arctic Oscillation." *Geophys. Res. Lett.,* **27,** 779–782.

Esler, J. G., and P. H. Haynes, 1999: Baroclinic wave breaking and the internal variability of the tropospheric circulation. *J. Atmos. Sci.,* **56,** 4014–4031.

Hartmann, D. L., and P. Zuercher, 1998: Response of baroclinic life cycles to barotropic shear. *J. Atmos. Sci.,* **55,** 297–313.

Haynes, P. H., 1989: The effect of barotropic instability on the nonlinear evolution of a Rossby-wave critical layer. *J. Fluid Mech.,* **207,** 231–266.

Hitchman, M. H., and A. S. Huesmann, 2007: A seasonal climatology of Rossby wave breaking in the 320–2000-K layer. *J. Atmos. Sci.,* **64,** 1922–1940.

Hoskins, B. J., I. N. James, and G. H. White, 1983: The shape, propagation, and mean-flow interaction of large-scale weather systems. *J. Atmos. Sci.,* **40,** 1595–1612.

Kidson, J. W., and I. G. Watterson, 1999: The structure and predictability of the "high-latitude" mode in the CSIRO9 general circulation model. *J. Atmos. Sci.,* **56,** 3859–3873.

Killworth, P. D., and M. E. McIntyre, 1985: Do Rossby-wave critical layers absorb, reflect or overreflect? *J. Fluid Mech.,* **161,** 449–492.

Leopard, P., 2006: A partition of the unit sphere into regions of equal area and small diameter. *Electron. Trans. Numer. Anal.,* **25,** 309–327.

Magnusdottir, G., and P. H. Haynes, 1996: Wave activity diagnostics applied to baroclinic wave life cycles. *J. Atmos. Sci.,* **53,** 2317–2353.

Martius, O., C. Schwierz, and H. C. Davies, 2007: Breaking waves at the tropopause in the wintertime Northern Hemisphere: Climatological analyses of the orientation and theoretical LC1/2 classification. *J. Atmos. Sci.,* **64,** 2576–2592.

McIntyre, M. E., and T. N. Palmer, 1985: A note on the general concept of wave breaking for Rossby and gravity waves. *Pure Appl. Geophys.,* **123,** 964–975.

Randel, W. J., and I. M. Held, 1991: Phase speed spectra of tran-

sient eddy fluxes and critical layer absorption. *J. Atmos. Sci.,* **48,** 688–697.

Riviere, G., and I. Orlanski, 2007: Characteristics of the Atlantic storm-track eddy activity and its relation with the North Atlantic Oscillation. *J. Atmos. Sci.,* **64,** 241–266.

Strong, C., and R. E. Davis, 2007: Winter jet stream trends over the Northern Hemisphere. *Quart. J. Roy. Meteor. Soc.,* **133,** 2109–2115.

——, and G. Magnusdottir, 2008: How Rossby wave breaking over the Pacific forces the North Atlantic Oscillation. *Geophys. Res. Lett.,* **35,** L10716, doi:10.1029/2008GL033578.

Thorncroft, C. D., B. J. Hoskins, and M. E. McIntyre, 1993: Two paradigms of baroclinic-wave life-cycle behaviour. *Quart. J. Roy. Meteor. Soc.,* **119,** 17–55.

Vallis, G. K., E. P. Gerber, P. J. Kushner, and B. A. Cash, 2004: A mechanism and simple dynamical model of the North Atlantic Oscillation and annular modes. *J. Atmos. Sci.,* **61,** 264–280.

Walker, C. C., and G. Magnusdottir, 2002: Effect of the Hadley circulation on the reflection of planetary waves in three-dimensional tropospheric flows. *J. Atmos. Sci.,* **59,** 2846–2859.

——, and ——, 2003: Nonlinear planetary-wave reflection in an atmospheric GCM. *J. Atmos. Sci.,* **60,** 279–286.

Waugh, D. W., and L. M. Polvani, 2000: Climatology of intrusions into the tropical upper troposhere. *Geophys. Res. Lett.,* **27,** 3857–3860.

Wernli, H., and M. Sprenger, 2007: Identification and ERA-15 climatology of potential vorticity streamers and cutoffs near the extratropical tropopause. *J. Atmos. Sci.,* **64,** 1569–1586.

Wittman, M. A. H., A. J. Charlton, and L. M. Polvani, 2005: On the meridional structure of annular modes. *J. Climate,* **18,** 2119–2122.

Woollings, T., B. Hoskins, M. Blackburn, and P. Berrisford, 2008: A new Rossby wave-breaking interpretation of the North Atlantic Oscillation. *J. Atmos. Sci.,* **65,** 609–626.